Journal of Rock Mechanics and Geotechnical Engineering 18 (2026) 4263–4277

Contents lists available at ScienceDirect

Journal of Rock Mechanics and Geotechnical Engineering

journal homepage: www.jrmge.cn

Full Length Article

Modelling thermomechanical fracturing in underground hydrogen storage in salt caverns

Hajar Habbani [a,*], Hippolyte Djizanne [a], Benoit Brouard [b], Amade Pouya [c]

[a] Ineris, The French National Institute for Industrial Environment and Risks, Verneuil-en-Halatte, 60550, France
[b] Brouard Consulting, Paris, 75003, France
[c] Navier Laboratory (UGE-ENPC-CNRS), Gustave Eiffel University, Champs-sur-Marne, 77420, France

ARTICLE INFO

Article history:
Received 31 March 2025
Received in revised form
21 January 2026
Accepted 10 February 2026
Available online 1 April 2026

Keywords:
Fracture mechanics
Salt cavern
Numerical computations
DISROC
Thermal fracturing
Hydrogen storage

ABSTRACT

In gas storage operations, intensive injection and withdrawal cycles can introduce structural failure due to thermally induced stresses, leading to the detachment of overhanging blocks from salt cavern walls. This study investigates the thermomechanical mechanisms governing block detachment in underground hydrogen storage using a joint enriched finite element method (JFEM) combined with cohesive zone modelling in DISROC software. An axisymmetric cavern geometry based on the Huntorf NK1 design is modelled, incorporating three overhanging blocks and both steady-state and transient creep components in the salt mechanical response. Comparative analysis of two salt types (fast-creeping Etrez and slow-creeping Asse) under identical thermomechanical loading reveals that rapid wall cooling during depressurisation (−13.8 bar/d) induces thermal contraction and tensile stresses exceeding rock salt tensile strength (1.5 MPa). Critical fracture initiation occurs at ~15 °C regardless of salt type, with block detachment sequences nearly identical between both salts (timing difference <6 h). The results demonstrate that thermal stresses (1 MPa/°C cooling) dominate failure mechanisms over steady-state creep, while transient creep accelerates stress redistribution and damage localisation. These findings highlight that temperature control, rather than creep properties, governs cavern stability, emphasising the critical need for thermal monitoring and controlled depressurisation rates in underground hydrogen storage operations.

© 2026 Institute of Rock and Soil Mechanics, Chinese Academy of Sciences. Published by Elsevier B.V. This is an open access article under the CC BY-NC-ND license (http://creativecommons.org/licenses/by-nc-nd/4.0/).

1. Introduction

Underground hydrogen storage (UHS) in salt caverns is a key option for balancing intermittent renewable energy supply. However, rapid pressure and temperature variations associated with injection/withdrawal cycles can generate intense thermo-mechanical stresses that threaten the cavern stability. Unlike progressive closure through creep, thermal contraction may induce tensile stresses that initiate fractures, leading to spalling or detachment of overhanging blocks.

Recently, finite-element analyses of fully coupled thermo-poroelastic behaviour have demonstrated significant alterations in local stress fields due to variations in drilling-fluid temperature and pressure in depleted reservoirs (Pirhadi et al., 2023, 2025). In a depleted limestone reservoir, cooling of the drilling fluid was shown to markedly increase the risk of tensile failure around the wellbore, whereas heating the fluid can mitigate tensile stresses and improve stability (Pirhadi et al., 2023). Further analysis of the Bangestan reservoir revealed that horizontal wells require a minimum compressive stress mud pressure of 57.23 MPa to remain stable, with an optimal 20 °C temperature offset between the formation and drilling fluid, thereby widening the safe operating window across different azimuths (Pirhadi et al., 2025). Complementing these pore-pressure and temperature effects, a scaling-up procedure converting dynamic elastic moduli from well logs into pseudo-static values has been introduced for precise calibration of temperature-dependent viscoplastic properties, establishing safe and stable mud-weight windows of 665-1900 kg/m^3 and 665-2499 kg/m^3, respectively, and reducing uncertainty in mechanical property calibration (Jamshidi et al., 2024).In addition,

* Corresponding author.
E-mail address: hajar.habbani@ineris.fr (H. Habbani).
Peer review under responsibility of Institute of Rock and Soil Mechanics, Chinese Academy of Sciences.

https://doi.org/10.1016/j.jrmge.2026.02.011
1674-7755/© 2026 Institute of Rock and Soil Mechanics, Chinese Academy of Sciences. Published by Elsevier B.V. This is an open access article under the CC BY-NC-ND license (http://creativecommons.org/licenses/by-nc-nd/4.0/).

systematic investigations have classified three distinct modes of cooling-induced thermal fracturing under different geometries and heat-conduction regimes. In a plane-strain model with one-dimensional heat conduction, single thermal fractures exhibit complex early-time growth before transitioning to a regime in which their length increases in proportion to the square root of the cooling time (Chen and Zhou, 2022). Around horizontal wells, radial transverse fractures initiate and coalesce under coupled thermo-poroelastic loading, with aperture evolution driven by thermal contraction and sensitive to fracture orientation and stress conditions (Chen and Zhou, 2025). Along vertical wells, two-wing and longitudinal fractures develop under anisotropic stress states, with dimensionless scaling laws for fracture length, spacing, and aperture as functions of cooling time and confining stress (Chen and Zhou, 2024).

Rock salt exhibits mechanical and thermal properties that are highly sensitive to temperature variations. Elevated temperatures accelerate creep, enhancing long-term cavern closure and surface subsidence, whereas cooling reduces creep rates but promotes brittle behaviour and tensile failure when thermally induced stresses exceed the low tensile strength of salt. In addition, the thermal conductivity of rock salt varies nonlinearly with temperature, which complicates the prediction of heat transfer within the formation during rapid cycling. These nonlinear and time-dependent effects strongly influence stress redistribution and damage evolution in the vicinity of cavern walls. Laboratory tests, in situ experiments, and operational evidence confirm rock salt sensitivity to cooling. Cyclic depressurisation has been shown to induce fractures in pellets and samples (Djizanne, 2014; Hévin et al., 2016) and to destabilise cavern walls in field experiments (Boucly and Legreneur, 1980). Several operational incidents (e.g. Kiel 101, Eminence, TE02, Jintan) further illustrate the potential for large-scale block falls under thermal-stress conditions. In contrast, long-term stable operation at Huntorf demonstrates that caverns can safely withstand frequent cycling when properly designed and monitored. A synthesis of these cases is provided in Table 1.

Although the creep behaviour of rock salt has been widely studied, the combined role of steady-state and transient creep in fracture development remains insufficiently explored. Moreover, while fracture mechanics has been applied to salt in simplified contexts, few studies have explicitly addressed block detachment under thermomechanical loading relevant to UHS.

The present study applies a joint-enriched finite element method (JFEM) with a cohesive zone model, implemented in DISROC, to simulate crack initiation, propagation, and block detachment in a cavern geometry with overhangs. The novelty lies in clarifying the mechanisms of thermally induced spalling and in distinguishing the respective roles of steady-state and transient creep. The results provide insight into block instability and safety margins for UHS operations.

2. Review of thermomechanical fracture mechanisms in salt caverns

Temperature variations in the fluids (brine, gas, etc.) inside a salt cavern cause the surrounding rock salt to heat up or cool down, leading to expansion or contraction. Because this deformation is partially constrained, thermal stresses develop and can result in spalling, collapse, or fracturing when significant temperature changes occur (Bérest et al., 2016). In salt caverns, a 1 °C drop in temperature induces approximately 1 MPa of additional tensile stress in the rock (Brouard et al., 2011). For an idealised shape (e.g. a sphere of radius a), the thermoelastic stress increment can be estimated analytically:

$$\Delta\sigma_{rr}(r) = \frac{-2\varpi}{r^3} I(r) \tag{1}$$

$$\Delta\sigma_{\theta\theta}(r) = \frac{\varpi}{r^3} I(r) - \varpi \Delta T_{\mathrm{salt}}(r) \tag{2}$$

$$\Delta\sigma_{zz}(r) = -\varpi \Delta T_{\mathrm{salt}}(r) \tag{3}$$

where $\Delta\sigma_{rr}$, $\Delta\sigma_{\theta\theta}$ and $\Delta\sigma_{zz}$ are thermoelastic additional radial, tangential, and vertical stresses, respectively, with $\varpi = E_{\mathrm{salt}}\alpha_{\mathrm{salt}}/(1-\nu_{\mathrm{salt}})$; E_{salt} and α_{salt} are the elastic parameters; α_{salt} is the thermal expansion coefficient; and $I(r) = \int_a^r u^2 \Delta T_{\mathrm{salt}}(u)\mathrm{d}u$.

In practice, these thermal stresses superimpose on the pre-existing geostatic stresses around the cavern, and if the total tensile stress exceeds the salt tensile strength, fractures can initiate.

2.1. Laboratory experiments

Experimental studies support the theoretical prediction that excessive cooling can lead to tensile fracturing of rock salt (Pellizzaro et al., 2011; Bérest et al., 2012). Djizanne (2014) conducted both microscopic- and macroscopic-scale laboratory tests on rock salt from French and German sites. In a micro-scale test, a small salt pellet was heated to 550 °C, then rapidly cooled to room temperature to induce thermal shock. Scanning electron microscopy (SEM) observations confirmed the initiation and propagation of open micro-cracks; by the end of cooling at 24 °C, the fractures showed significantly larger openings compared to those observed at 222 °C (Fig. 1). In a macro-scale test, a 2 m block of salt was uniformly heated to ~90 °C before its surface was exposed to cold air from a vortex gun. This cooling produced a strong thermal gradient across the block. No visible macroscopic cracks developed (total crack opening was only ~0.3 mm), but deformation monitoring revealed alternating bands of localised contraction and dilation near the cooled surface, oriented perpendicular to the

Table 1
Documented cases of thermomechanical instabilities in salt caverns.

Case/location	Depth (m)	Pressure/temperature change	Observed effect	Source
Kiel 101 (Germany)	1305-1400	$\Delta P = -6.6$ MPa in 5 d (−1.3 MPa/d)	Roof failure, volume loss	Röhr (1974); Bérest et al. (2012)
Eminence Dome (USA)	1725-2000	Cyclic ΔP = 6-28 MPa; repeated cycles	40% volume loss; 36 m bottom rise	Coates et al. (1983); Bérest et al. (1986)
TE02 (France)	650-900	9 cycles between 8 and 22 MPa; T = 32 °C-69 °C	1/3 vol loss; 5.8 m bottom rise	Boucly and Legreneur (1980)
JK-A (China)	~1700	$\Delta P = -5.4$ MPa in 18 d	Roof collapse (~3300 m^3)	Wang et al. (2018)
Gorleben shafts (Germany)	Near surface	$\Delta T \approx -20$ °C over 80 d	Vertical and horizontal fractures (mm aperture)	Wallner and Eickemeier (2001); Zapf et al. (2012)
Huntorf NK1 (Germany)	650-800	ΔP up to 5 MPa/h; ΔT cycles	Long-term stability; minor collapses	Crotogino et al. (2001); Djizanne et al. (2014)

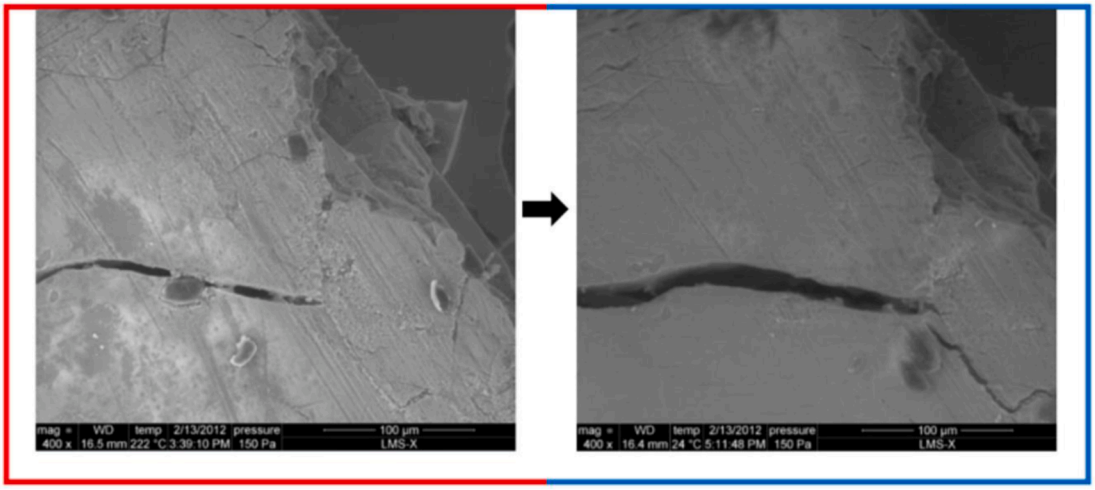


Fig. 1. Observation of the appearance and evolution of cracks after cooling using an SEM (Djizanne, 2014).

airflow. These bands were attributed to the low thermal conductivity at the salt/air interface, causing steep temperature gradients and non-uniform strain in the near-surface layer.

2.2. Field tests

The STARFISH in situ experiment in the Varangéville salt mine investigated the effects of rapid cooling on a 10 m^2 area of cavern wall (Hévin et al., 2016). The salt rock was subjected to cyclic temperature variations: each cooling phase lasted 28 d, lowering the wall temperature from ~15 °C to −9 °C (a 24 °C drop across ~1.5 m of salt), followed by a heating phase back to 15 °C. Over three such cycles, thermal stresses induced networks of vertical cracks about 1 m deep with apertures <1 mm (Fig. 2b). Partial crack closure was observed upon reheating due to thermal expansion of the salt, indicating a reversible component to the damage. Numerical modelling of the test confirmed that the crack patterns corresponded to tensile-stress zones induced by the imposed thermal gradients (Hévin et al., 2016). Another classic field test by Dreyer (1977) involved leaching a small cavern (2 m × 1 m) at a depth of 600 m and filling it with liquid nitrogen at −196 °C. The extreme cooling generated large tensile stresses in the surrounding rock, leading to the formation of several fractures perpendicular to the cavern wall. Four major cracks remained visible at the end of the test (Dreyer, 1977), demonstrating the cavern-damaging potential of rapid cooling.

2.3. Real cavern incidents

Several real-world cases illustrate how pressure and temperature fluctuations influence salt cavern stability, often leading to cavern shrinkage, block falls, or roof collapse. In the Gorleben salt mine, for example, Wallner and Eickemeier (2001) observed fractures in air intake shafts after an exceptionally cold winter lowered the air temperature by ~20 °C below the rock temperature for 80 d. The thermal contraction induced significant tensile stresses, opening vertical and horizontal fractures with millimetre apertures spaced ~2.8 m apart. Finite element analyses with discrete fracture elements later confirmed that the temperature differential caused the fracture opening, which partially closed

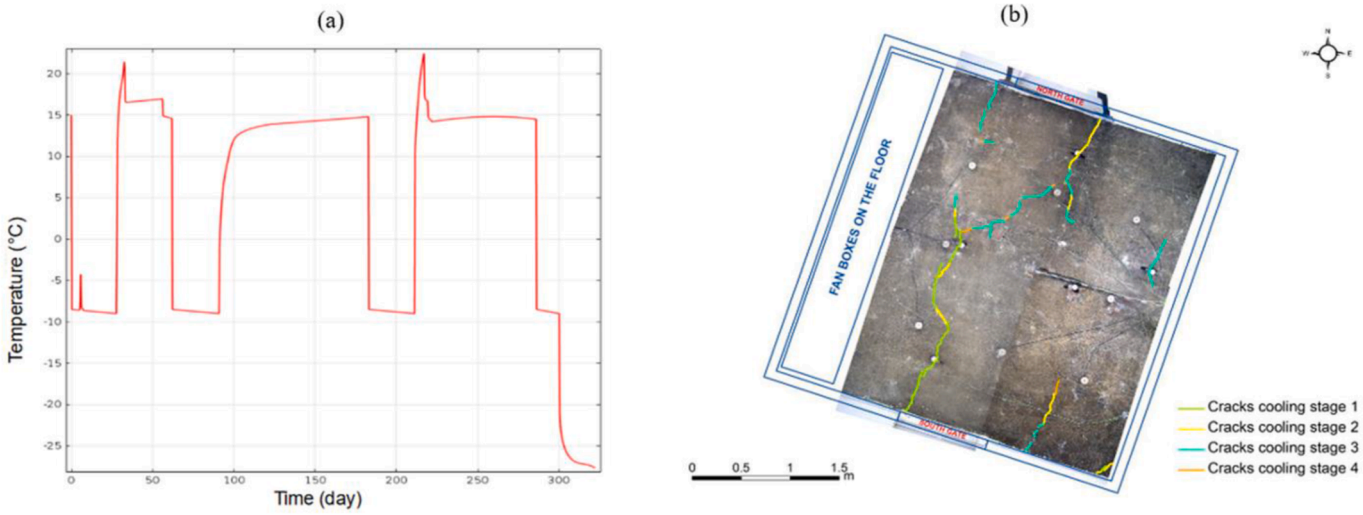


Fig. 2. (a) Change of room air temperature during the experiment, and (b) Map of cracks reactivated and created during the fourth cooling stage (Hévin et al., 2016).

upon warming (Zapf et al., 2012).

Rapid pressure drops can likewise trigger instability. The Kiel 101 cavern in Germany (depth: 1305-1400 m) experienced a roof failure during a pressure test. The cavern pressure was reduced from ~13.1 MPa to 6.5 MPa over 5 d (withdrawal rate: ~1.3 MPa/d). Following this, sonar surveys revealed a substantial decrease in the cavern volume. This suggests that sudden depressurisation, together with the heterogeneous salt surrounding the cavern and a large insoluble accumulation, led to a roof block fall (Röhr, 1974; Bérest et al., 2012). A similar phenomenon was documented in Eminence Cavern #1 (Mississippi, USA, depth of 1725-2000 m). After the cavern underwent repeated pressure cycles between ~6 MPa and 28 MPa, a sonar survey in 1972 revealed ~40% volume loss and a 36 m rise of the cavern floor, indicating significant collapse of the salt structure (Coates et al., 1983). Bérest et al. (1986) suggested that asymmetric deformation was exacerbated by higher overburden pressure and temperature in the lower part of the cavern, thereby contributing to instability.

In France, the Tersanne TE02 cavern (depth of ~1400-1550 m) was leached in 1968-1970 to a volume of ~91,600 m^3. It experienced nine cyclic pressure drops from 22 MPa to 8 MPa (with temperature cycling between ~32 °C and 69 °C) over 1970-1979. By mid-1979, significant shrinkage was evident: the cavern bottom had risen ~5.8 m. After refilling with brine, a sonar showed the cavern volume had reduced by one-third (to ~58,200 m^3). The damage was attributed to a combination of block falls from the walls/roof and creep closure. This early field evidence underscores the compounded effect of pressure cycling and thermal stresses on cavern convergence and integrity (Boucly and Legreneur, 1980).

A more recent incident occurred at Jintan (JK-A) in China, where a large gas storage cavern (~50 m span) suffered a roof collapse of 2-4 m thick (~3300 m^3 fallen) between 2009 and 2015. The failure followed a rapid pressure drop from 15.8 MPa to 10.4 MPa in 18 d, which critically lowered the dilatancy safety factor of the salt (Wang et al., 2018). The presence of weak interlayers (anhydrite, clayey dolomite, glauberite) near the cavern roof likely intensified the stress concentrations, contributing to the collapse.

While many caverns have experienced such thermomechanical instabilities, others have shown long-term operational success. The Huntorf **C**AES caverns in Germany, for instance, have operated for decades under frequent air pressure cycles (about 4.3-7 MPa, with depressurisation rates up to 5 MPa/h) with only minor signs of damage. Sonar surveys of the Huntorf NK1 cavern revealed a 16 m floor rise due to salt curtain collapses early in its life (Quast, 1983), but no major roof falls occurred thereafter (Crotogino et al., 2001). Numerical studies by Djizanne et al. (2014) examined mechanisms like brine buoyancy during debrining in the Huntorf cavern. Their analysis indicated that during debrining (removal of brine after leaching), the tensile effective stress within the overhanging blocks remained nearly zero, suggesting that block detachment did not initiate under this loading condition. In the present paper, we focus on overhanging block falls in a Huntorf-type cavern filled with hydrogen, using JFEM to evaluate fracture initiation and propagation under realistic thermomechanical cycling.

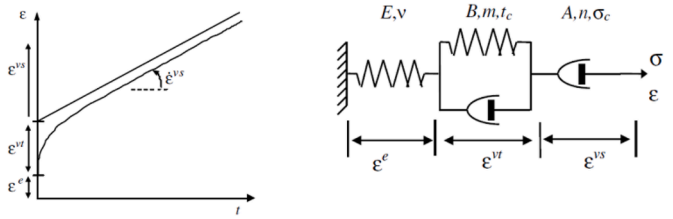


Fig. 3. Double mechanism creep law principle developed by Pouya (1991).

3. Constitutive modelling

To accurately capture the complex thermomechanical behaviour observed in real-world cases, appropriate constitutive models must be employed. The following sections detail the mechanical behaviour of rock salt and the fracture-mechanics framework required to simulate overhanging block detachment under the thermal loading conditions identified above.

3.1. Creep behaviour of rock salt

The mechanical behaviour of rock salt exhibits significant nonlinearity depending on stress type and duration. Under short-term loading, rock salt shows elastic-ductile behaviour in compression and elastic-brittle behaviour in tension. Over extended periods, it undergoes viscous flow, characterised as an elasto-viscoplastic material with significant temperature sensitivity. The total strain rate comprises elastic, viscoplastic, and thermal contributions (Bérest, 2011):

$$\dot{\varepsilon} = \dot{\varepsilon}^{\mathrm{el}} + \dot{\varepsilon}^{\mathrm{vp}} + \dot{\varepsilon}^{\mathrm{th}} \tag{4}$$

$$\dot{\varepsilon}^{\mathrm{el}} = \frac{1+\nu}{E}\dot{\sigma} - \frac{\nu}{3E}\dot{\sigma}_{kk}\delta \tag{5}$$

$$\dot{\varepsilon}^{\mathrm{th}} = \alpha \dot{T}_{\mathrm{salt}}\delta \tag{6}$$

3.1.1. Steady-state creep

Salt steady-state creep follows the Norton-Hoff (N-H) power law, establishing relationships among strain, deviatoric stress, and temperature under steady-state conditions. The strain rate increases with temperature following the Arrhenius law (Norton, 1929). The power law exponent (n) typically ranges from 3 to 5, characterising rock salt as a non-Newtonian viscous fluid where strain rate depends nonlinearly on deviatoric stress J_2:

$$\dot{\varepsilon}^{\mathrm{vp}} = \frac{3}{2} A\, e^{-\left(\frac{Q}{RT}\right)} \left(\sqrt{3J_2}\right)^{n-1} \sigma \tag{7}$$

where A is a material constant, Q is the activation energy, R is the gas constant, T is the temperature, n is the stress exponent, and σ is the deviatoric stress tensor. The N-H law stipulates that the strain rate under constant loading approaches steady-state values (Bérest and Brouard, 1998).

3.1.2. Double mechanism creep

The conventional Arrhenius formulation fails to capture experimental variations over broad temperature ranges, as creep acceleration exceeds model predictions (Pouya, 1991). Alternative approaches include summing two Arrhenius expressions (Langer, 1981) or incorporating polynomial temperature dependence (Tijani, 1989).

Theoretical reflections on microphysical deformation mechanisms support the existence of steady-state creep phenomena

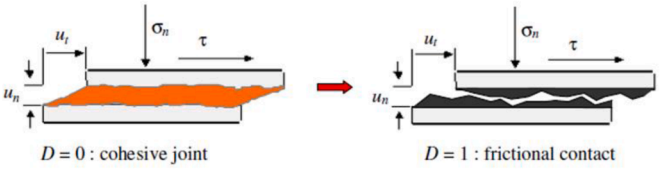


Fig. 4. Damage degradation of the single joint cohesive zone (Trivellato et al., 2018).

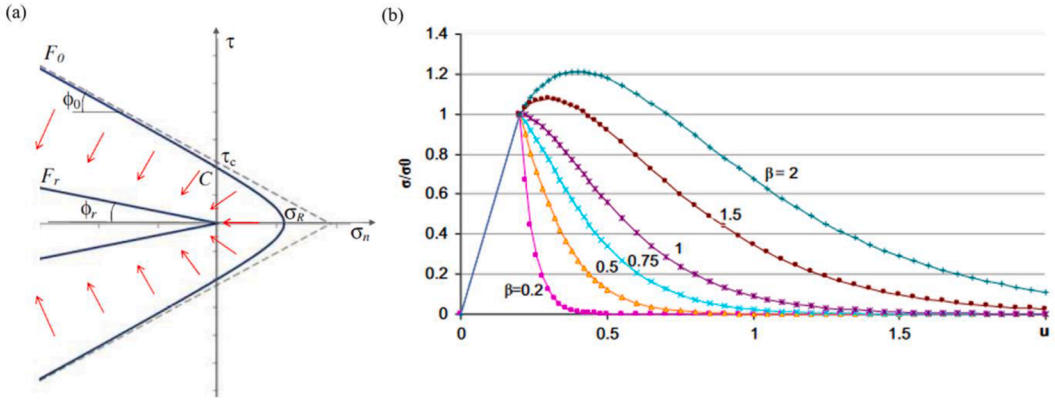


Fig. 5. (a) Stress-displacement in the cohesive zone model for different β values, and (b) Evolution of the damage criterion to full joint failure (Ouraga et al., 2017).

Table 2
Parameters for joint elements.

Parameter	Symbol/Unit	Value	Source
Normal stiffness	K_{nn} (MPa. m^{-1})	300,000	Claystone analogue
Shear stiffness	K_{tt} (MPa. m^{-1})	300,000	Claystone analogue
Residual aperture	e_0 (m)	0.01	Numerical stability
Tensile strength	σ_t (MPa)	1.5	Grgic et al. (2022)
Cohesion	C (MPa)	8	Coarita-Tintaya et al. (2023)
Friction angle	ϕ (°)	36.8	Coarita-Tintaya et al. (2023)
Fracture toughness	K_{IC} (MPa.m$^{1/2}$)	0.85	Wang et al. (2016)
Ductility parameter	β	0.1	Pouya and Bemani (2015)
Scaling condition	$L > (2/\pi)(K_{IC}/\sigma_t)^2$	Applied	Fracsima (2016)

(Munson and Dawson, 1982; Langer et al., 1984). Under constant loading, the internal structure changes until reaching new stable states after transient phases. This requires complementing steady creep (N-H law) with transient models:

$$\dot{\varepsilon}^{vp} = \dot{\varepsilon}^{vt} + \dot{\varepsilon}^{vs} \tag{8}$$

The steady-stress creep $\dot{\boldsymbol{\varepsilon}}^{vs}$ is given by Eq. (4) below, and the transient creep $\dot{\boldsymbol{\varepsilon}}^{vt}$ corresponds to a limited creep deformation with a decreasing rate. For uniaxial deformation starting at $t = 0$ under constant stress σ, transient creep follows:

$$\varepsilon^{vt}(t) = b\sigma^m \left(1 - e^{-\frac{t}{t_c}}\right) \tag{9}$$

The general transient creep rate tensor is

$$\dot{\boldsymbol{\varepsilon}}^{vt} = \frac{3}{2}\dot{\varepsilon}^{vt}\frac{\boldsymbol{S}}{\sigma_e} \tag{10}$$

where $s\left(=\sigma\sigma_{ij} - \frac{1}{3}\sigma_{kk}\delta\right)$ is the deviatoric stress tensor, and $\sigma_e = \sqrt{3J_2}$ is the von Mises equivalent stress. The scalar function $\dot{\varepsilon}^{vt}$ satisfies

$$\dot{\varepsilon}^{vt}(t) = \frac{1}{t_c}\left(\varepsilon^{*vt} - \varepsilon^{vt}\right) \tag{11}$$

where b, m and t_c are the material parameters; $\varepsilon^{*vt} = b\sigma_e^m$ represents the maximum transient creep; and t_c is the characteristic time. Parameters b, m and t_c are material-dependent, with b potentially temperature-dependent as $b = Be^{-Q/RT}$. The characteristic time t_c follows the rule: at $t = 3t_c$, the transient creep reaches 95% of the maximum value.

This dual mechanism captures both the immediate deformation response (transient creep) and the long-term steady flow (Fig. 3), which are essential for accurate thermomechanical analysis under varying conditions.

3.2. Fracture mechanics

While the viscoplastic behaviour described above governs the bulk deformation of rock salt, fracture initiation and propagation require additional modelling approaches. For instance, when the Bérest effective stresses exceed the material tensile strength, localised failure occurs, necessitating damage mechanics formulations to capture crack development and block detachment.

Progressive weakening of rock strength and stiffness leads to fractures, which are modelled using damage mechanics with cohesive zone elements representing potential crack paths. Fractures follow the cohesive fracture approach (Barenblatt, 1962), where a cohesive zone model (CZM) provides a phenomenological description of interface separation during crack propagation.

In this model, cohesive elements are introduced along expected crack paths between solid matrix elements. A narrow cohesive zone with vanishing thickness exists ahead of the crack tip, characterising the fracture process zone (Jin and Sun, 2006). Upper and lower surfaces act as cohesive surfaces, deforming according to a constitutive law linking the stress tensor ($\underline{\sigma}$) to relative displacements ($\underline{u}$) between surfaces. In two-dimensional analysis, both components are normal and tangential.

Crack propagation occurs when separation at the cohesive zone trailing edge exceeds critical thresholds defined by the specified failure criteria. A key advantage is the elimination of stress singularities at crack tips, which are inherent in classical linear elastic fracture mechanics (Dugdale, 1960; Barenblatt, 1962).

Damage mechanic characterises progressive deterioration using the cohesive fracture framework of Pouya and Bemani (2015). Internal damage variable D quantifies degradation at each potential discontinuity, represented numerically as joint elements.

Table 3
Cavern geometrical properties.

Volume (m^3)	Brine volume (%)	Hydrogen volume (%)	Cavern height (m)	Cavern top (m)	Cavern bottom (m)	Average depth (m)
329,489	0.04	99.96	150	650	800	725

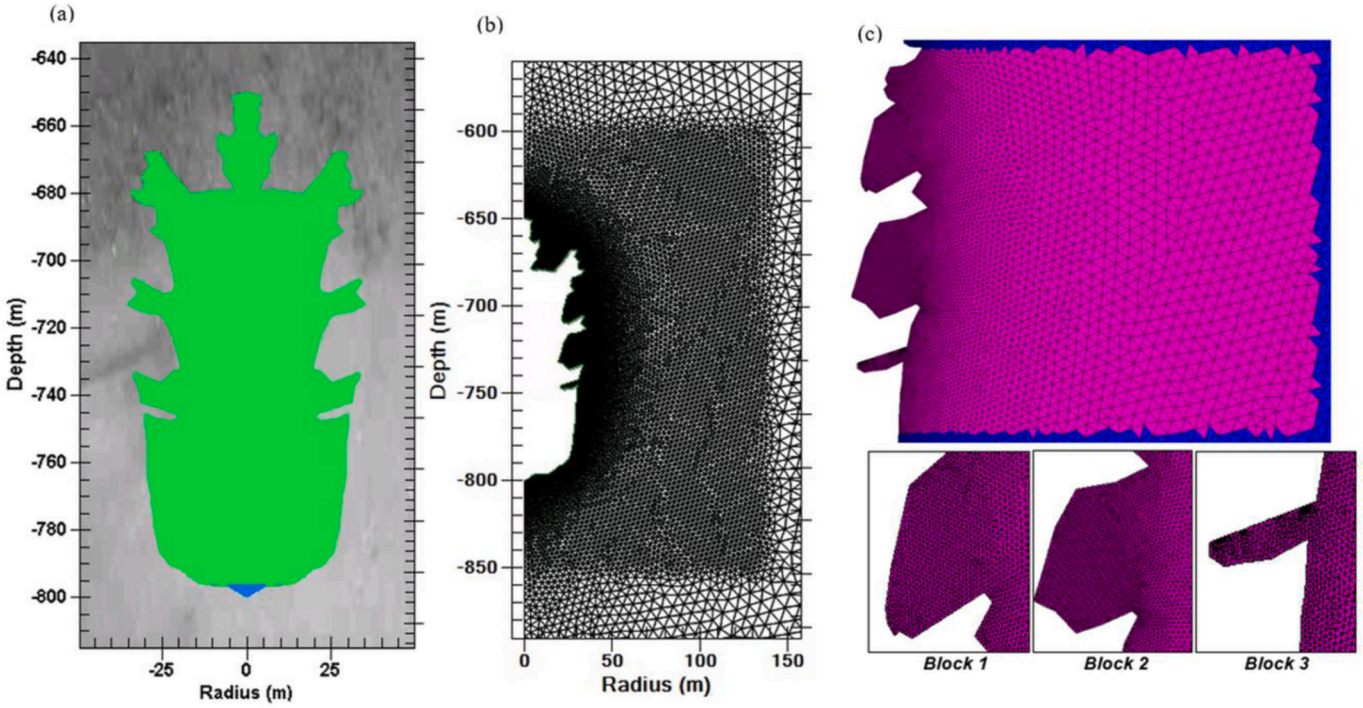


Fig. 6. (a) The Huntorf NK1 sonar inspires the cavern shape, (b) Cavern meshing model, and (c) Joint elements area.

Following initial yielding ($D = 0$), the material degrades until complete cohesive zone failure ($D = 1$), signifying fracture initiation. At this stage, discontinuity emerges in the displacement field (Fig. 4).

The damage-based constitutive law relating to kinematic and static variables is

$$\underline{\sigma} = \begin{pmatrix} \tau \\ \sigma_n \end{pmatrix} = (1-D)\cdot K \cdot \underline{u} + s \cdot k_0 \cdot \underline{u}\,; \quad \underline{u} = \begin{pmatrix} u_t \\ u_n \end{pmatrix} \tag{12}$$

Parameter s is a binary contact indicator: $s = 0$ denotes no contact between fracture surfaces, while $s = 1$ signifies contact. The damage cohesive model enforces non-penetration ($u_n > -e_0$, where e_0 represents the joint aperture). Intact material stiffness K undergoes degradation governed by D, while residual stiffness k_0 applies when $D = 1$:

$$K = \begin{pmatrix} K_{tt} & 0 \\ 0 & K_{nn} \end{pmatrix};\ k_0 = \begin{pmatrix} k_{0t} & 0 \\ 0 & \dfrac{k_{0n}}{\left(1+\frac{u_n}{e_0}\right)^2} \end{pmatrix} \tag{13}$$

The model utilises hyperbolic yield surfaces, ensuring smooth transitions from pure normal/shear mode failure to mixed modes (Fig. 5a, $D = 0$). This model distinguishes two critical crack initiation situations (Carol et al., 1997): (1) Mode I: Pure tension with no shear stresses; and (2) Asymptotic mode II: Shear under high compression approaching the Coulomb criterion.

The failure criterion for cohesive fractures (Pouya and Bemani, 2015, Fig. 5a) depends on tangential stress, normal stress, and damage.

At the yield point, fractures may also develop in a mixed mode, positioned between the initial threshold modes. The failure criterion for cohesive fractures, as proposed by Pouya and Bemani (2015) (Fig. 5a), is expressed as a function of tangential stress, normal stress, and damage, and is formulated as follows:

Table 5
Huntorf plant specifications.

Specification	Value (bar)
Minimum permissible cavern pressure	1
Minimum operational exceptional cavern pressure	20
Minimum operational regular cavern pressure	43
Maximum permissible and operational cavern pressure	70

Table 4
Hydrogen thermodynamic properties.

C_p (J/(mol K))	C_v (J/(mol K))	Dynamic viscosity (Pa s)	Compressibility	M (g/mol)
14.831	10.714	0.85×10^{-5}	1.001	2.016

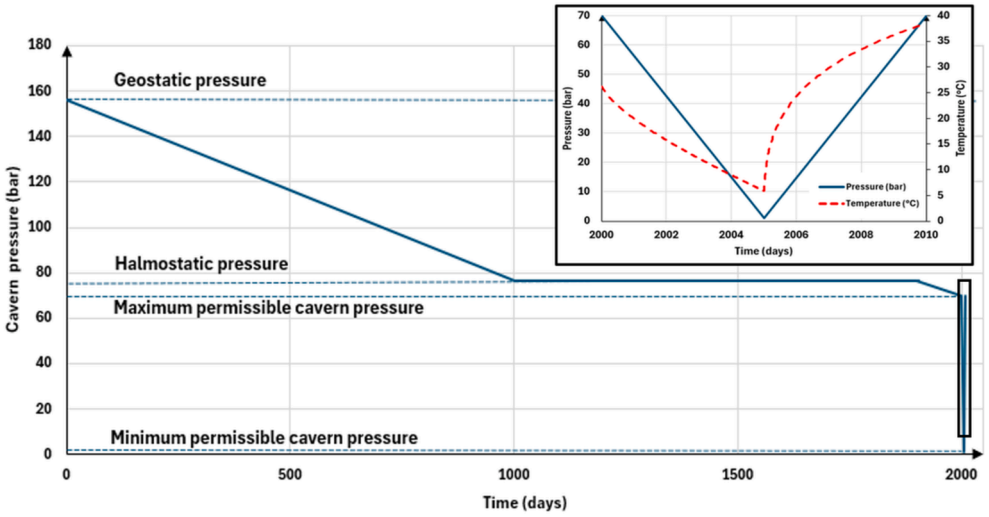


Fig. 7. Pressure evolution at the cavern top (The depressurisation rate is −13.8 bar/d).

$$\left.\begin{aligned}(\tau,\sigma_n,D) &= \tau^2 - {\sigma_n}^2\tan^2\varphi + 2g(D)\tau_c\sigma_n - g^2(D)C^2\\ \tau_c &= \frac{C^2+\sigma_R^2\tan^2\varphi}{2\sigma_R}\end{aligned}\right\} \quad (14)$$

where C represents the cohesion, φ is the friction angle, and σ_R is the limit tensile strength. Function $g(D)$ from consistency conditions is

$$g(D) = (1-D)[1-\beta\ln(1-D)] \quad (15)$$

Damage variable D evolution is governed by the elastic displacement limit u_0. When the normal displacement u_n exceeds u_0, D grows exponentially (Fig. 5b):

$$D = 1 - e^{-\frac{u_n-u_0}{\beta u_0}} \quad (u_n \geq u_0) \quad (16)$$

Parameter β defines material ductility (0 to ∞): high β corresponds to ductile materials, and $\beta = 0$ represents brittle behaviour.

The constitutive law requires 10 parameters: K_{tt}, K_{nn}, σ_t, C, ϕ, k_{0t}, k_{0n}, β, e and K_{IC} (Table 2). Normal and tangent stiffnesses K_{tt}, K_{nn}), minimal aperture (e), and ductility parameter (β) are based on Callovo-Oxfordian claystone data (Fallah Soltanabad et al., 2023) due to comparable quasi-brittle behaviour and stiffness range. Tensile strength (σ_t), cohesion (C), and friction angle (ϕ) adopt laboratory values from Grgic et al. (2022). Fracture toughness uses the energy release rate $G_{IC} = 22$ J/m^2 recommended for salt (Silberschmidt and Silberschmidt, 2000), with K_{IC} calculated via Irwin's relation using elastic parameters $E = 30$ GPa, and $\nu = 0.25$.

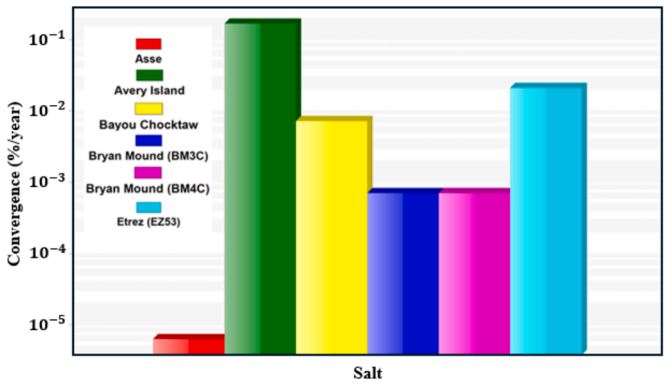


Fig. 8. N.-H. convergence rate of a cylindrical cavern, $P = 85.3$ bar, $T = 31.3$ °C, source: LOCAS.

4. Numerical modelling

The constitutive laws presented above are implemented within the DISROC finite element framework to simulate the thermo-mechanical response of salt caverns. The following sections describe the geometric model, boundary conditions, and loading scenarios used to investigate the stability of an overhanging block under hydrogen storage conditions.

4.1. Geometrical model

Numerical modelling is performed using DISROC (Fracsima, 2016), a finite element code enriched with joint elements for coupled thermo-hydromechanical analysis in fractured media. Its pre-processor, DISCRAC, generates conforming meshes with zero-thickness joint elements, eliminating the need for remeshing during fracture growth. The software incorporates advanced constitutive models, including viscoplasticity and cohesive-zone interface laws for mixed-mode fracture propagation (Pouya and Bemani, 2015).

An axisymmetric hydrogen-filled cavern measuring 150 m high and 71 m wide, located at 650 m depth, is examined. The design is based on the Huntorf NK1 cavern, known for its overhanging block structure (Quast, 1983; Djizanne et al., 2014). Geometrical properties are summarised in Table 3.

Based on Brouard et al. (2011), for high-frequency cyclic loading, the thermally disturbed zone thickness adjacent to cavern walls increases with cycling period τ according to

$$\Delta r = 2.9\times10^4\sqrt{\pi\frac{k_{salt}\tau}{2}} \quad (17)$$

where Δr is in centimetres, k_{salt} is the diffusivity of rock salt (m^2/s), and τ is in days. Temperature peaks persist near walls, requiring fine discretisation. The maximum radial element size is set to $\Delta x_{max} = \Delta r/5$, within a near-wall layer of thickness $2\Delta r$.

The mesh comprises three regions: a high-density zone near cavern walls (5 m thick) with a maximum spacing of 0.5 m, a moderate-density zone with elements up to 3 m, and a low-density zone with elements up to 10 m (Fig. 6b). The total mesh contains 52,828 elements, including triangular and joint elements.

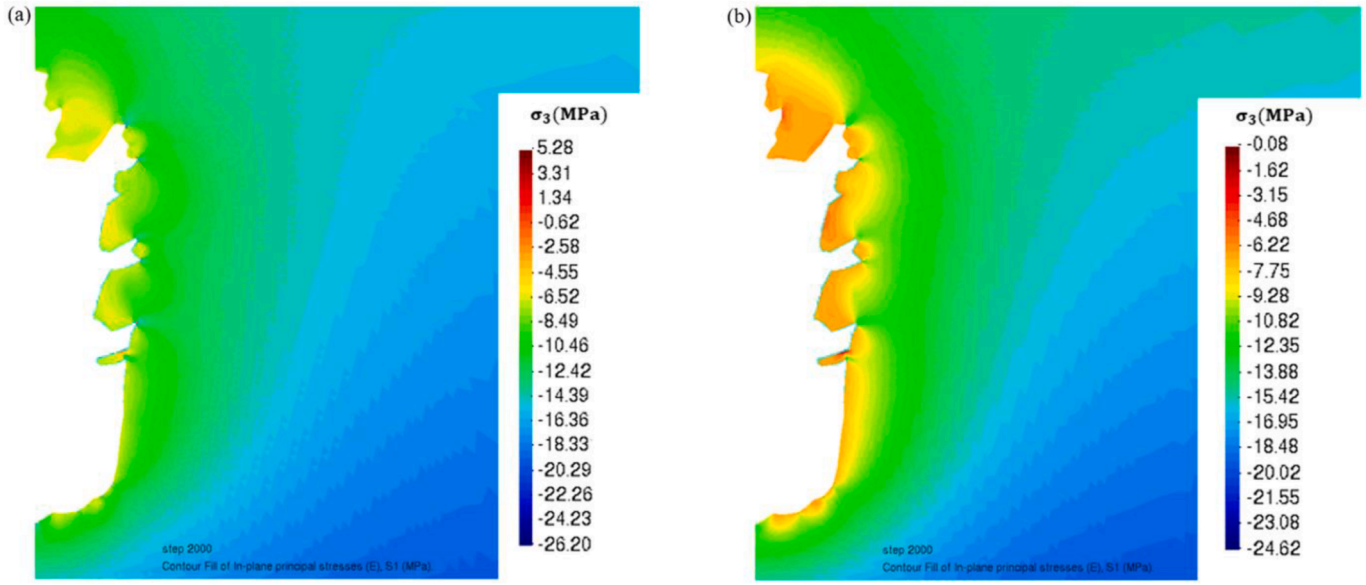


Fig. 9. Least compressive stress contour plot at the end of debrining: (a) Etrez salt, and (b) Asse salt.

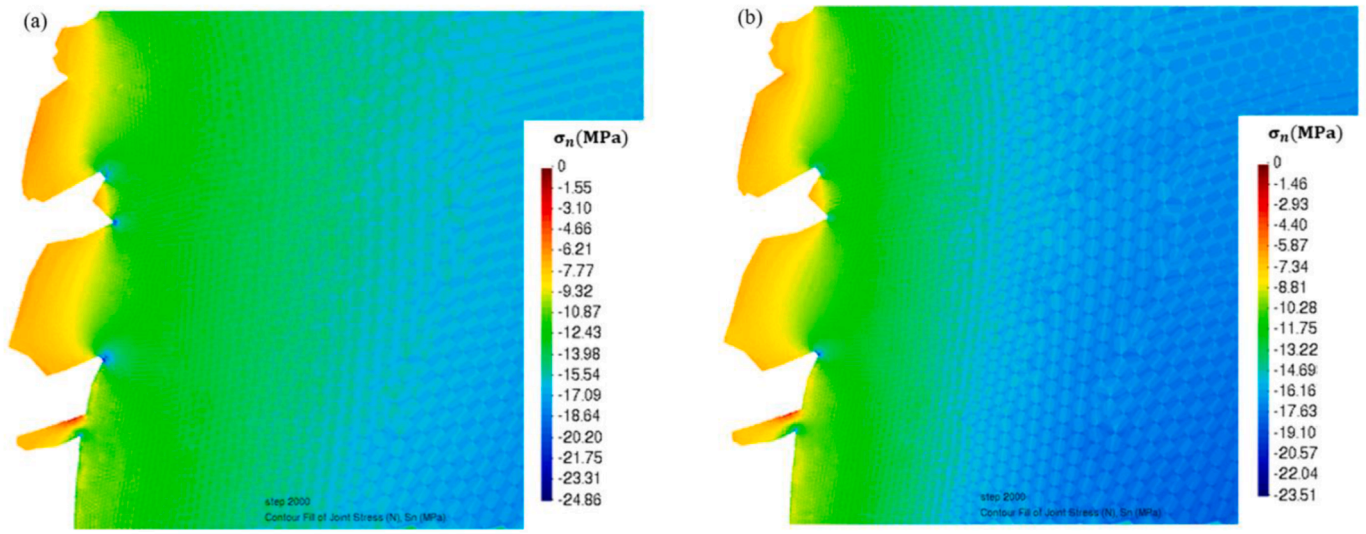


Fig. 10. Joint normal stress contour plot at the end of debrining: (a) Etrez salt, and (b) Asse salt.

Joint elements are generated near the cavern walls, encompassing three overhanging blocks (Fig. 6c), to simulate the nucleation and propagation of cracks.

DISCRAC enables node splitting and joint element creation for displacement discontinuities (Tounsi et al., 2020). To eliminate mesh-size bias, toughness-based regularisation is used where material toughness fixes fracture energy, and DISROC rescales joint peak traction and cohesion with element length L, ensuring mesh-independent energy dissipation by

$$L > \frac{2}{\pi}\left(\frac{K_{IC}}{\sigma_t}\right)^2 \tag{18}$$

4.2. Boundaries and initial conditions

The axisymmetric model applies thermomechanical loading with specified boundary conditions: vertical displacement is constrained to zero along the bottom surface, radial displacement is set to zero along the axis of revolution, and geostatic pressure is applied along the outer radius. Ground-level temperature is 10.98 °C with a bottom heat flux of 99.8 mW/m^2. The geothermal temperature and geostatic pressure at the cavern mid-depth are 31.3 °C and 166.5 bar, respectively.

4.3. Hydrogen properties

Gaseous hydrogen properties for conditions 293.15 K and 1 atm (1.01325 bar) are presented in Table 4, with thermodynamic computations using Lemmon et al. (2008) state equations.

4.4. Thermomechanical loading

Loading conditions comply with Huntorf cavern specifications (Crotogino et al., 2001) outlined in Table 5.

The withdrawal-injection cycle models critical scenarios encompassing maximum and minimum permissible pressures (Fig. 7). The sequence includes: (1) halmostatic pressure

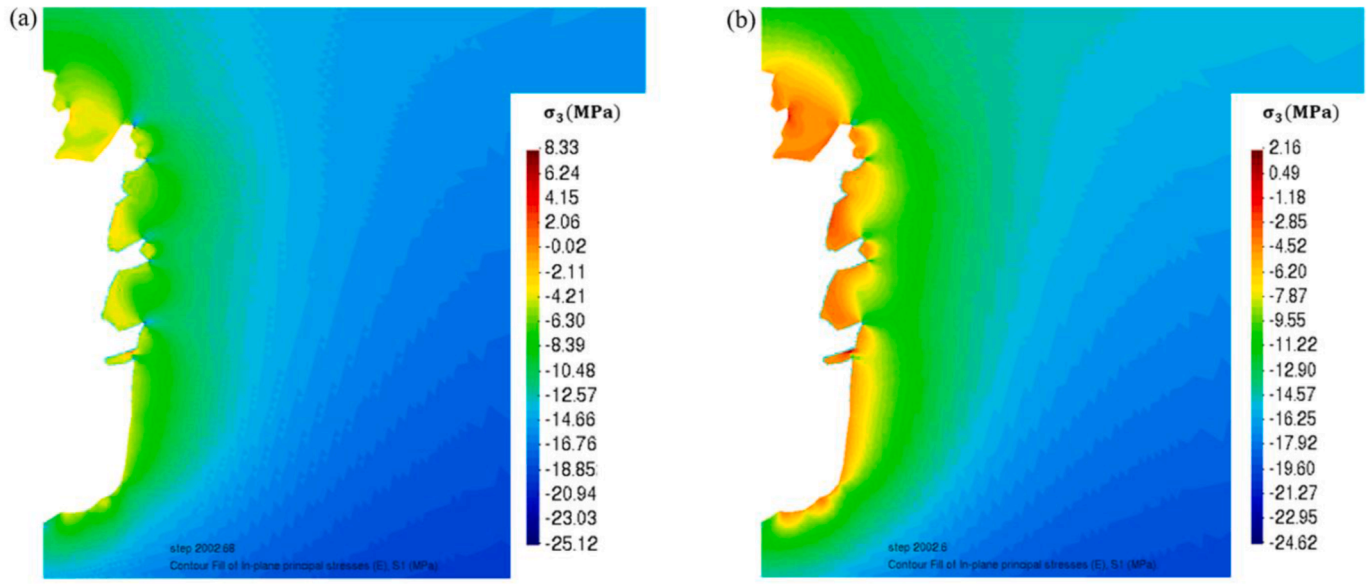


Fig. 11. Contour plot of the least compressive stress during the withdrawal phase: (a) Etrez salt at 2.68 d, and (b) Asse salt at 2.6 d.

application post-leaching, (2) 100-d debrining to maximum pressure, (3) 5-d withdrawal to minimum pressure, and (4) 5-d injection phase.

The temperature evolution follows LOCAS calculations (Brouard et al., 2022) for the thermomechanical behaviour of a hydrogen-filled cavern. During leaching, the temperature drops from the geothermal temperature (31.3 °C) to the brine temperature (25 °C).

Time increment adaptation prevents convergence issues from viscoplastic components. The viscoplastic strain rate $\dot{\varepsilon}_{\mathrm{vp}}$ adaptively controls the increment Δt to preserve quasi-static equilibrium. The maximum viscous strain rate over all Gauss points $E_{\mathrm{M}}^{\mathrm{vp}} = \max_i \|\dot{\varepsilon}_{\mathrm{vp},i}\|$ determines Δt such that the viscous strain increment remains below the prescribed bound $\Delta\varepsilon_{\mathrm{vp}} = 10^{-5}$:

$$\Delta t = \Delta\varepsilon_{\mathrm{vp}} / E_{\mathrm{M}}^{\mathrm{vp}} \tag{19}$$

The creep rate governs step size: the time increment decreases when the creep rate is high and increases as the creep rate decreases.

5. Results and discussion

Using the thermomechanical loading protocol described above, numerical simulations are conducted to investigate the mechanisms of fracture initiation and block detachment. The analysis first examines steady-state creep behaviour before incorporating transient effects to provide a comprehensive understanding of failure processes.

5.1. Steady-state creep

This section presents a block fall analysis for two rock salt types: Etrez salt (Bérest and Brouard, 1998), exhibiting higher convergence rates and greater creep susceptibility, and Asse salt (Wawersik, 1984), characterised by lower convergence and stable mechanical response (Fig. 8). The analysis focuses on steady-state creep governed by the Norton-Hoff law to assess how cavern convergence influences fracture initiation and overhanging block falls.

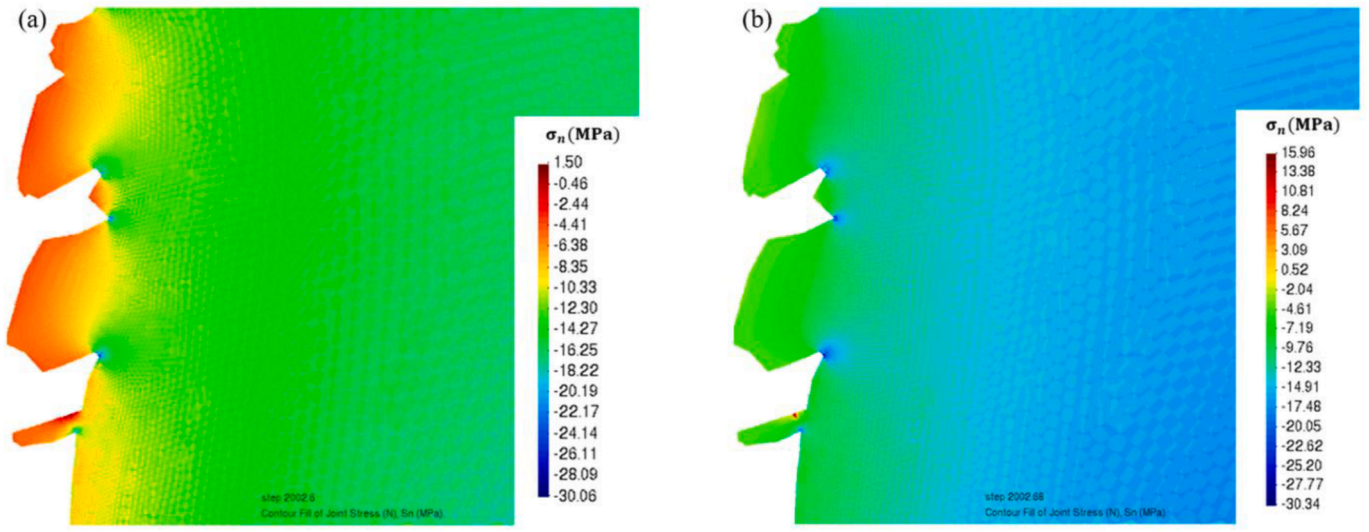


Fig. 12. Joint normal stress contour plot during the withdrawal phase for Etrez salt: (a) Before fracture initiation at 2.6 d, and (b) Onset of fracture at 2.68 d.

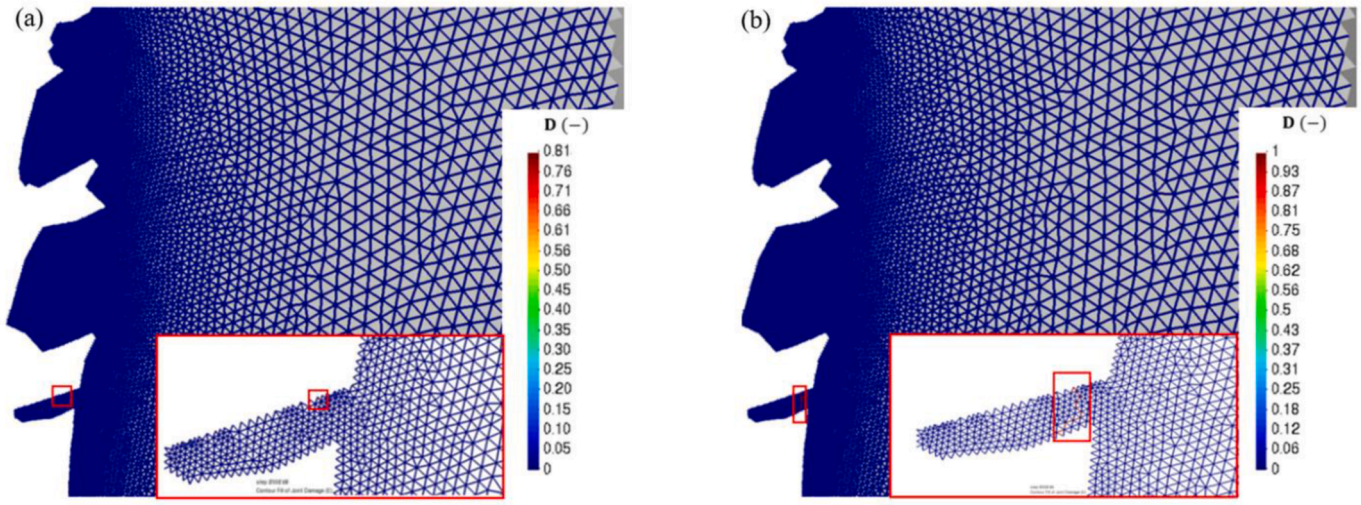


Fig. 13. Evolution of the induced fracture zone during the withdrawal phase for Etrez salt: (a) Onset of fracture at 2.68 d, and (b) End of fracture propagation at 2.7 d.

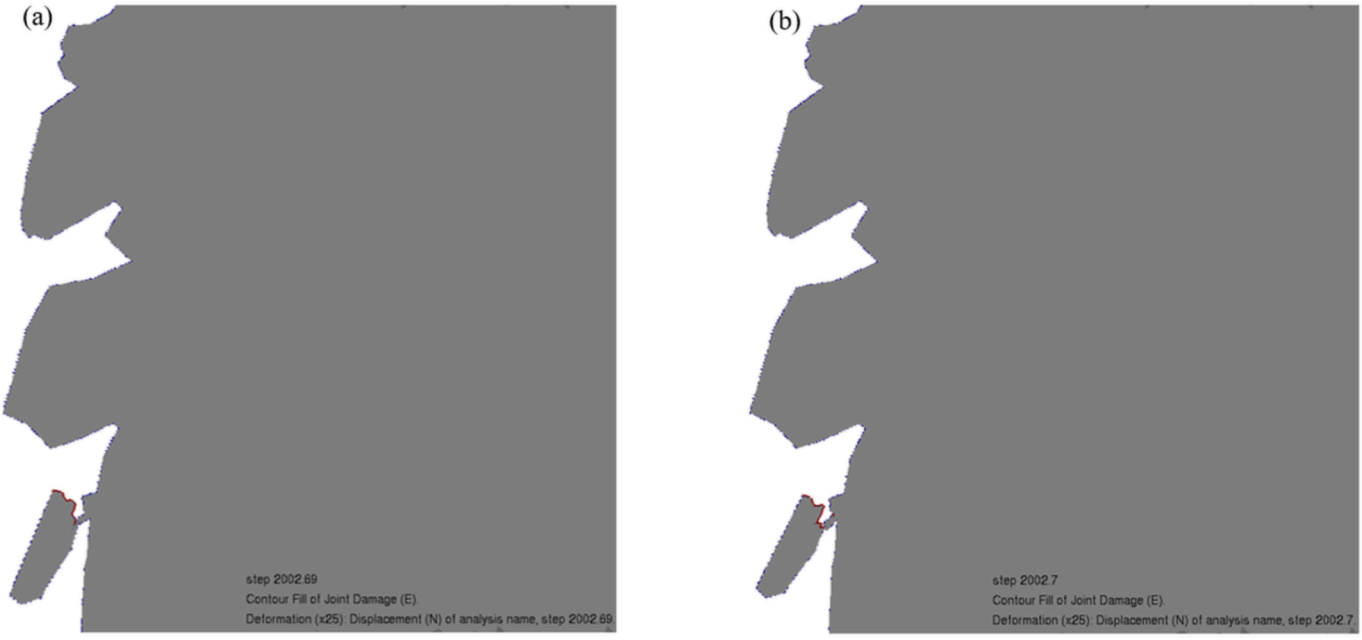


Fig. 14. Overhanging block 3 falling for (a) Etrez salt and (b) Asse salt (×25 deformation).

5.1.1. At the end of debrining

During debrining, cavern pressure decreases slightly from halmostatic to maximum allowable pressure (Fig. 7), while the temperature increases from 25 °C to 26.13 °C. Fig. 9 shows stress variations, with red zones indicating tensile stress and blue regions representing compressive stress.

For Etrez salt (Fig. 9a), localised tensile zones ($\sigma_3 > 1.5$ MPa) appear near cavern walls and overhanging blocks, with peak values reaching 5.28 MPa. Stress transitions gradually with increasing compression toward deeper sections ($\sigma_3 \approx -26$ MPa), suggesting a higher fracture risk. Conversely, Asse salt (Fig. 9b) exhibits limited tensile zones with peak stress of −0.08 MPa (below the tensile strength), indicating greater stability. Compressive stress distribution is more uniform, reaching −24.62 MPa in deeper regions.

To assess block stability using fracture mechanics, normal stress at joints is analysed relative to the tensile strength threshold. Fig. 10 shows that while blocks 1 and 2 remain in compression, block 3 transitions into tension ($\sigma_n = 0$ MPa) but stays below the failure threshold. No fracture initiation is expected at this stage.

5.1.2. Withdrawal phase onset (13.8 bar/d)

During the 5-d withdrawal, cavern pressure drops from 70 bar to atmospheric while temperature decreases from 26.13 °C to 3.86 °C. Fig. 11 highlights fracture initiation zones.

For Etrez salt (Fig. 11a), tensile stress develops in block 3, reaching $\sigma_3 = 1.45$ MPa at 2.68 d (temperature: 14.69 °C). For Asse salt (Fig. 11b), $\sigma_3 = 2.16$ MPa at 2.6 d (temperature: 14.95 °C), indicating the onset of fracture.

Fig. 12a shows the normal stress distribution reaching the tensile strength at 2.6 d in block 3 for Etrez salt. After fracture initiation (Fig. 12b), the normal stress in the newly formed joint rises to 15.96 MPa, triggering stress redistribution and relaxation

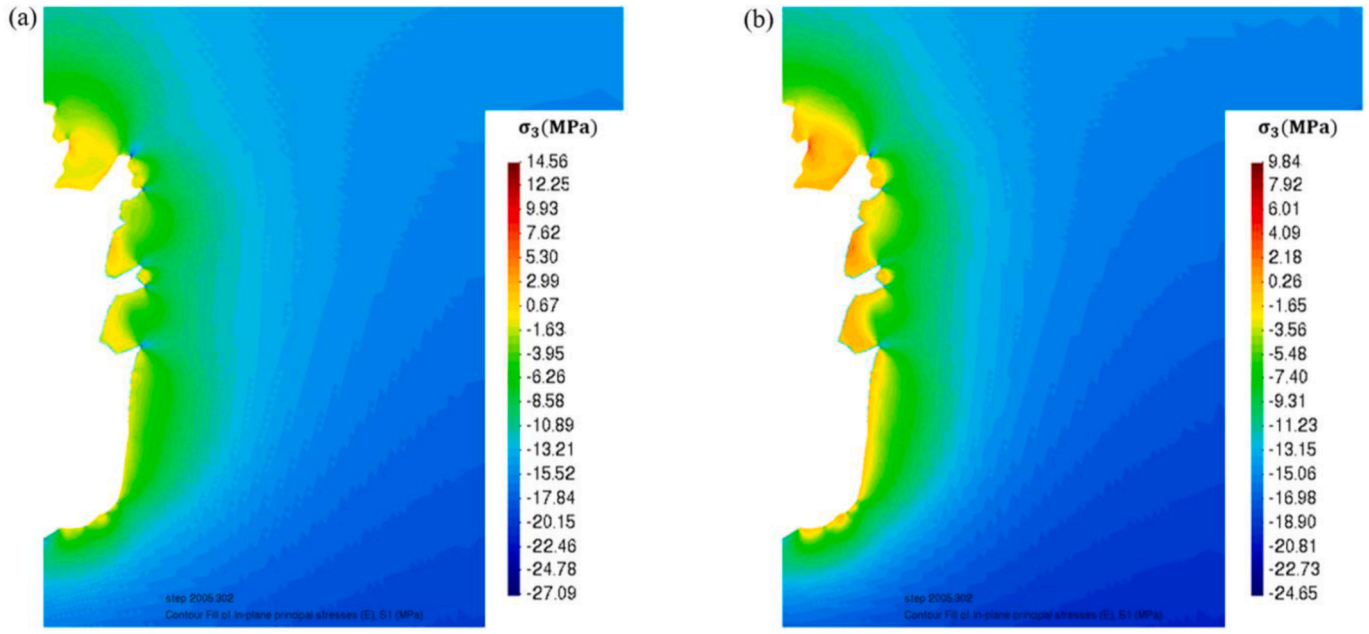


Fig. 15. Least compressive stress during the withdrawal phase (4.3 d): (a) Etrez salt, and (b) Asse salt.

in adjacent blocks (from −0.46 MPa to −4.89 MPa).

Crack initiation occurs when the normal stress exceeds the tensile strength while the joint remains partially intact ($D = 0.81$), leading to brittle failure (Fig. 13a). Between 2.6 d and 2.68 d, the progressive crack propagation occurs, reaching complete joint failure ($D = 1$), as shown in Fig. 13b.

5.1.3. Block 3 detachment

Fig. 14 depicts block 3 detachment due to unstable crack propagation at 2.69 d (Etrez) and 2.7 d (Asse). Despite minor timing differences, fracture paths remain similar, suggesting steady-state creep is not the primary detachment driver. Instead, thermal stress differentials from rapid cooling (22 °C in 5 d) trigger thermal-induced fractures.

5.1.4. At the end of withdrawal phase (13.8 bar/d)

Following the detachment of block 3, the simulation continues to evaluate the stability of the remaining overhanging blocks under continued thermal loading. After block 3 detachment, Fig. 15 shows potential fracture zones in the remaining blocks. Following initial fracturation, tensile stress increases significantly: for Etrez salt, σ_3 rises from 1.45 MPa (2.68 d) to 8.87 MPa (4.3 d); for Asse salt, from 2.16 MPa to 8.95 MPa, following comparable evolution patterns. Temperature drops to 6.90 °C, corresponding to 7.79 °C cooling for Etrez and 8.05 °C for Asse salt.

Fig. 16 shows the joint normal stress distribution after 4.3 d of withdrawal. The maximum normal stress reaches 15.50 MPa (Etrez) and 15.82 MPa (Asse), over 10 times the tensile strength, and is concentrated at the extremity of block 1. Following fracture onset, damage reaches $D = 0.84$ (Asse) and $D = 0.82$ (Etrez), triggering stress redistribution and compressive relaxation at cavern walls.

Fig. 17 illustrates the evolution of fracture in the Asse salt, beginning at 4.3 d with stable propagation transitioning to unstable penetration, resulting in significant damage at 4.4 d. Fig. 18 shows minimal differences in fracture length between salt types,

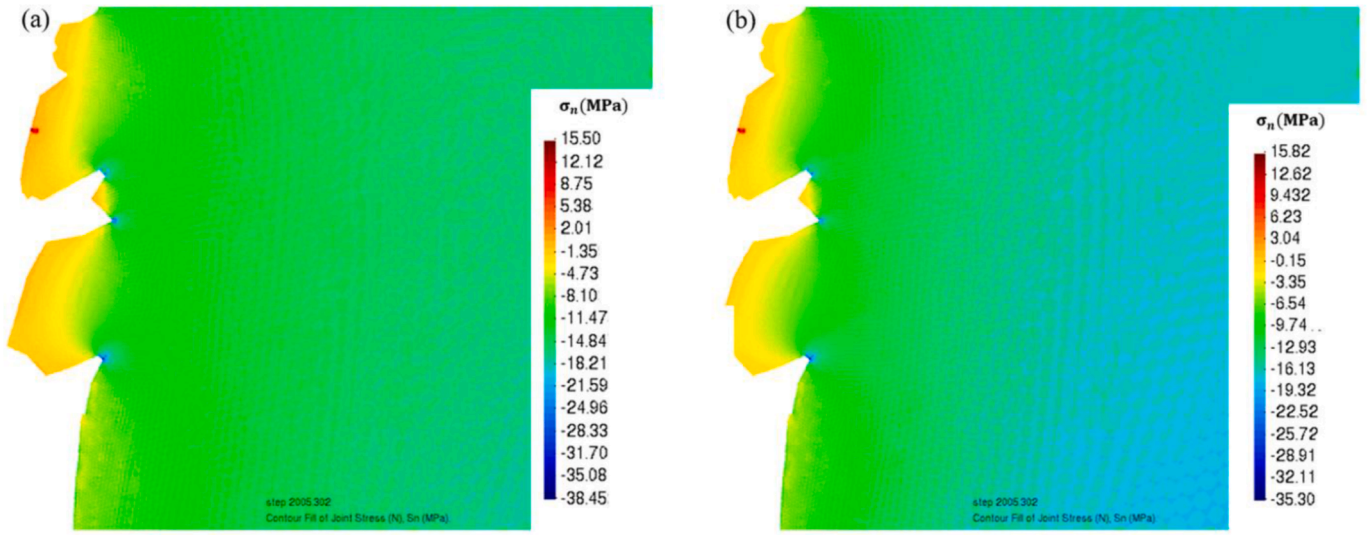


Fig. 16. Joint normal stress contour plot at withdrawal phase (4.3 d) for (a) Etrez salt and (b) Asse salt.

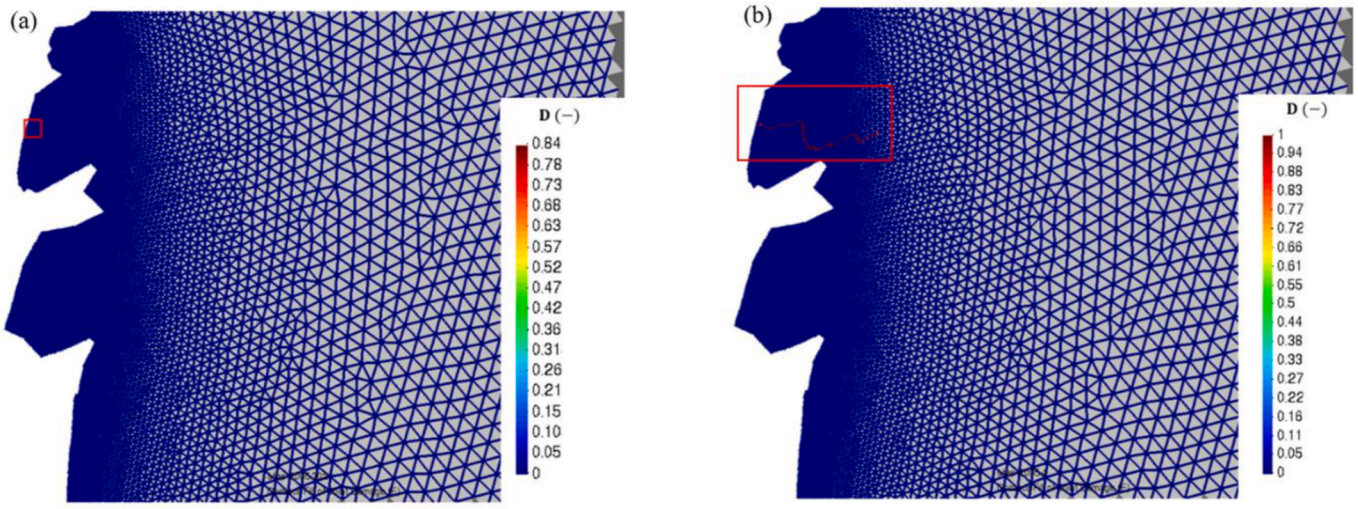


Fig. 17. Evolution of the induced fracture zone during the withdrawal phase for Asse salt: (a) Onset of fracture and (b) end of fracture propagation at 4.4 d.

reinforcing the conclusion that thermal stress dominates over creep-induced convergence.

5.2. Double mechanism creep

The steady-state creep analysis demonstrates the dominance of thermal effects over long-term creep deformation. To further investigate the role of transient behaviour, the following section incorporates both primary and secondary creep mechanisms, revealing additional insights into stress redistribution and damage localisation during the early phases of cavern operation.

This section incorporates transient and stationary creep components using the Pouya (1991) constitutive model. Transient creep parameters for Etrez salt are listed in Table 6.

During the leaching simulation, geostatic pressure decreases to the halmostatic pressure over 1000 d while temperature drops from 31.3 °C to 25 °C, inducing large stress variations.

Fig. 19 compares stress distributions at the leaching end (Fig. 19a) and the beginning of the stand-by process (Fig. 19b). At leaching completion, the least compressive stress reaches 0.66 MPa in block 3. During stand-by, stress increases to $\sigma_3 \approx 6$ MPa, amplifying local deformations and triggering fracture initiation.

Fig. 20 presents the evolution of joint normal stress and fracture propagation. The normal stress significantly exceeds the tensile strength, reaching $\sigma_n = 11.46$ MPa (Fig. 20a), which causes unstable propagation due to excessive energy dissipation (Fig. 20b).

Transient creep exacerbates cavern wall fracturing by increasing deviatoric stress through leaching, thereby activating accelerated creep mechanisms. Primary creep exhibits higher deformation rates than steady-state creep, causing rapid stress redistribution. This generates localised stress concentrations that promote the formation and propagation of microcracks.

5.3. Discussion on salt types and mechanisms

A key finding of this study is that the salt steady-state creep rate (fast vs. slow creep) has a limited effect on short-term fracturing behaviour under rapid cycling. Table 7 summarises the comparative outcomes between the Etrez and Asse salt simulations. Both salts initiate cracking at approximately the same cavern wall temperature (~15 °C), and both undergo block detachment almost simultaneously (within a few hours of each other). Etrez

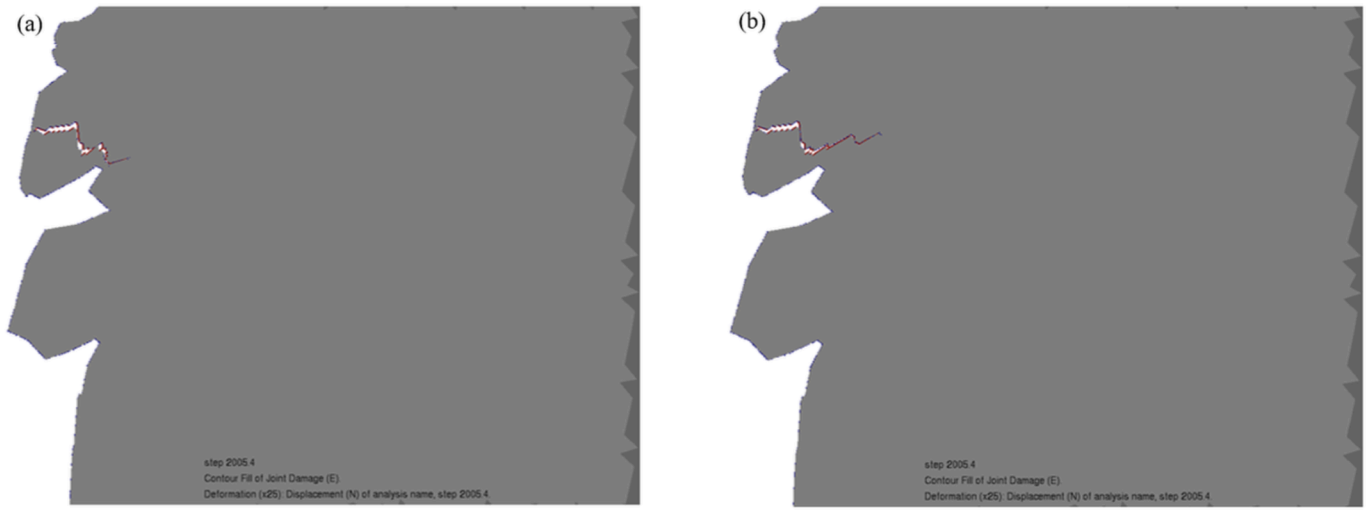


Fig. 18. Detachment of overhanging block 1 for (a) Etrez salt and (b) Asse salt with ×25 deformation.

Table 6
Sets of parameters for Etrez rock salt.

Rock salt	A (MPa^{-n}/yr)	Q/R (K)	t_c (h)	n	m	b
Etrez	0.64	4100	0.01	3.1	3.9	0.77

salt, being more compliant in creep, showed slightly earlier tensile stress development and micro-cracking, but Asse salt, despite creeping less, ultimately suffered the same block detachment once the thermal stress reached critical levels. Transient creep (when included) accelerated fracture initiation in both salts but did not substantially alter the time of block separation. This comparative analysis reinforces the notion that thermal stresses predominate over creep deformation in causing these rapid failure phenomena. In practical terms, a "fast-creeping" salt cavern (like Etrez) and a "slow-creeping" one (like Asse) would both be at risk if subjected to an excessively rapid depressurisation, as the thermal shock can induce spalling regardless of differences in long-term creep closure rates.

The comparative analysis reveals similarities in the thermo-mechanical response between Etrez and Asse salts during withdrawal operations. Regarding tensile stress onset, Etrez exhibits tensile zones only a few hours earlier than Asse during withdrawal, yet both salt types reach the critical tensile failure threshold of approximately 1.5 MPa when cavern wall temperatures drop to around 14 °C-15 °C.

Once thermal tensile stress exceeds the material strength, fractures initiate in identical locations for both salt types, specifically at the bases of overhanging blocks. While Etrez demonstrates a slightly higher peak tensile stress, typically 0.1-0.2 MPa greater than Asse just before cracking occurs, this difference stems from its greater creep relaxation in other regions rather than

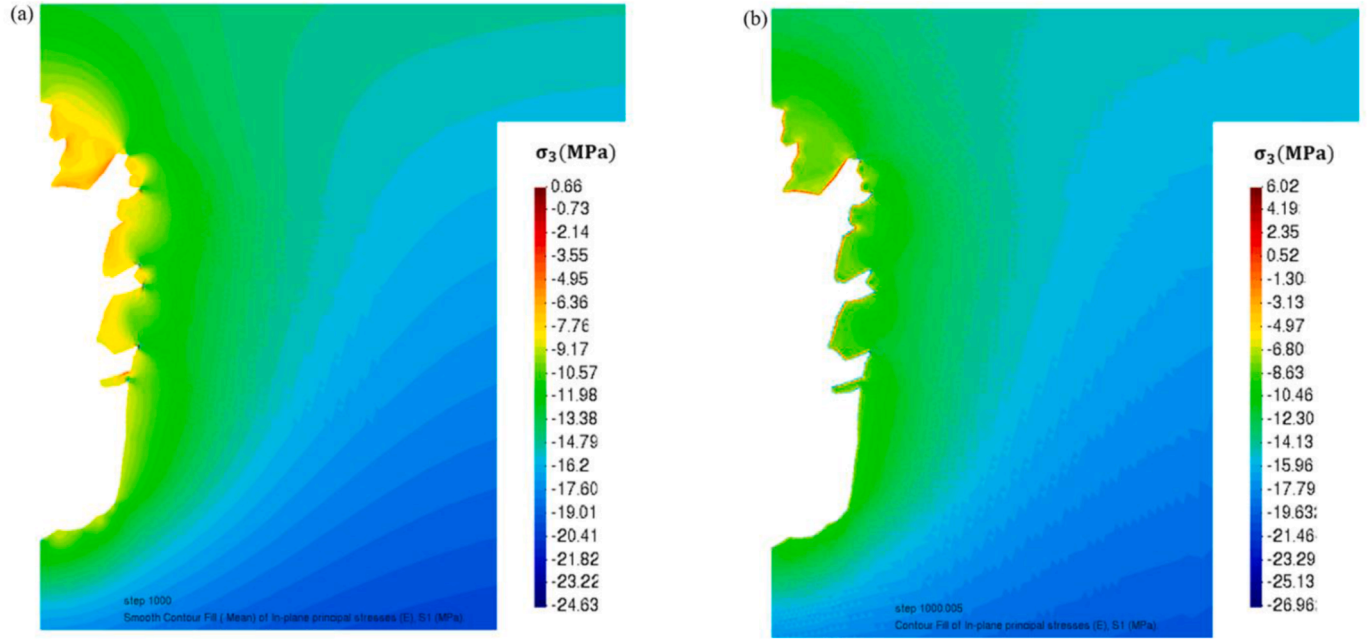


Fig. 19. Contour plot of the least compressive stress (σ_3) for Etrez salt (a) at the end of leaching and (b) at the beginning of the stand-by process.

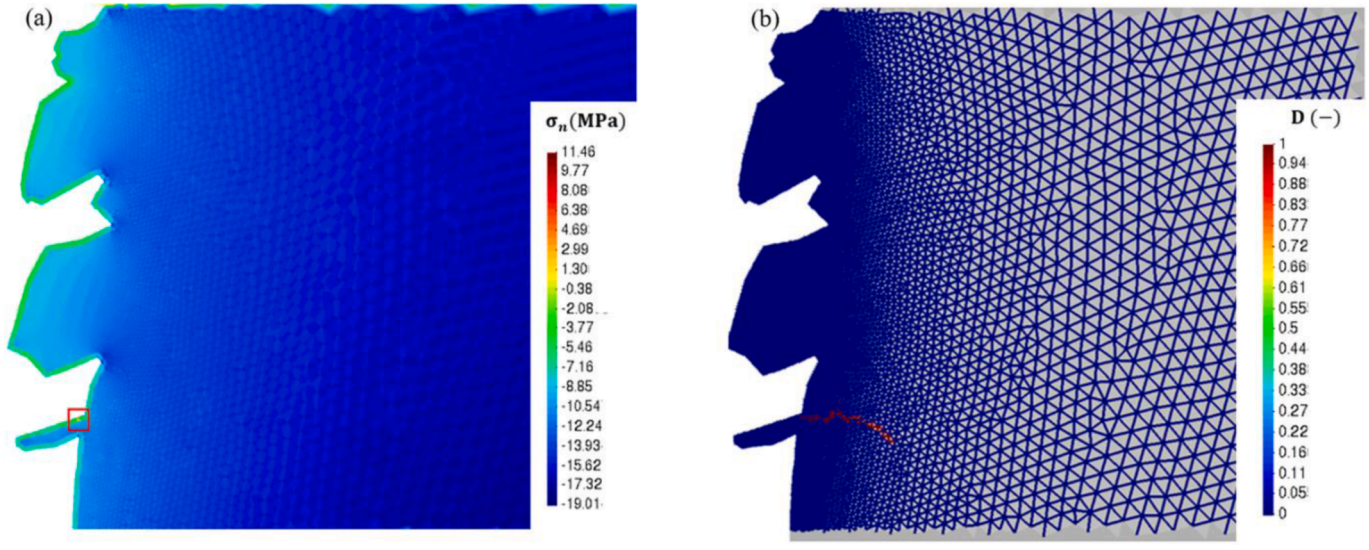


Fig. 20. Joint normal stress contour plot at the onset of fracture (a) and damage field contour at the end of fracture propagation (b).

Table 7
Comparison of results between fast-creeping (Etrez) and slow-creeping (Asse) salt caverns under rapid withdrawal.

Condition	Etrez salt	Asse salt	Comment
Convergence rate	Higher	Lower	Etrez more creep-prone
End of debrining ($T \approx 26$ °C)	Tensile zones at the wall	Compression-dominated	Instability risk in Etrez
Withdrawal ($\Delta P = -13.8$ bar/d; $\Delta T \approx -22$ °C)	$\sigma_3 \approx +1.45$ MPa at 2.68 d	$\sigma_3 \approx +2.16$ MPa at 2.6 d	Earlier fracture in Etrez
Block 3 detachment	2.69 d	2.70 d	Very similar sequence
Post-detachment stress (4.3 d)	$\sigma_3 \approx +8.9$ MPa	$\sigma_3 \approx +9.0$ MPa	Comparable stress buildup
Fracture mode	Thermal stress-driven	Thermal stress-driven	Mode independent of creep rate

fundamental differences in fracture mechanics. Notably, the crack propagation path remains essentially identical in both materials, indicating that thermal stress gradients, rather than creep properties, govern, in this case, the fracture development process.

The timing of final block detachment provides perhaps the most compelling evidence for thermal dominance over creep effects. The detachment of the largest overhanging block occurs at virtually the same time in both computational models, approximately 2.7 d into the withdrawal phase. The temporal difference between Etrez and Asse salt detachment was less than 6 h, representing a negligible variation considering the different creep characteristics of these materials.

The role of creep mechanisms proved limited in influencing the overall fracture sequence under rapid cooling conditions. While steady-state creep differences between fast-creeping Etrez and slow-creeping Asse were significant under normal operational conditions, these differences had minimal impact on the fracture sequence when subjected to rapid thermal variations. Transient creep accelerated stress redistribution and microcrack formation in both cases, but neither delayed nor prevented the eventual block detachment; instead, it primarily facilitated rather than controlled the failure process.

Following block detachment, both salt types exhibited comparable stress re-equilibration patterns. The least compressive principal stress rose to approximately 8-9 MPa in the remaining structural pillars for both materials, indicating similar post-failure response mechanisms despite their differing creep properties. This stress redistribution behaviour reinforces the conclusion that thermal effects dominate the mechanical response during rapid operational cycles, with creep properties playing a secondary role in determining the overall structural behaviour of the cavern system. Even a salt type known for its stability (like Asse) can experience block detachment if subjected to a sufficiently rapid pressure drop, leading to strong cooling. Conversely, mitigating thermal shocks (by slowing depressurisation or preheating the gas) should significantly reduce the risk of spalling, even in faster-creeping salts.

6. Conclusions

The simulations demonstrate that rapid gas withdrawal (and the associated cooling) generates tensile thermal stresses that are the dominant cause of crack initiation and overhanging block detachment in salt caverns. In our models, a cooling rate of −14 °C/d at the cavern wall induced about 1 MPa of tensile stress per °C, quickly exceeding the ~1.5 MPa tensile strength of rock salt and leading to fracture. This result indicates that temperature drops during depressurisation pose the primary hazard to hydrogen cavern integrity, rather than long-term creep deformations.

A comparative analysis of a fast-creeping salt (Etrez) and a slow-creeping salt (Asse) under identical loading conditions revealed nearly identical failure sequences. Steady-state creep differences (which affect long-term convergence) had little influence on the short-term fracturing outcome. Transient creep, on the other hand, played a noticeable but secondary role; it accelerated stress redistribution and micro-cracking before the main fracture event, but it did not ultimately prevent or significantly delay the block detachment. In both salt types, the largest overhanging block failed at roughly the same time and at the same wall temperature. Thus, thermal shock conditions govern failure, while creep (especially steady-state creep) mainly affects how stress builds up rather than the outcome.

These findings underscore the crucial need to control thermal and pressure conditions in hydrogen storage operations. The rate of change in pressure and temperature also influences cavern stability. To avoid thermomechanical damage, such as spalling and block falls, operators should implement controlled depressurisation rates and actively monitor cavern temperature. Real-world cases support this: incidents of block fall were linked to rapid cycling, whereas facilities like Huntorf remained stable under more moderate, controlled cycling. Future cavern designs and operating protocols should prioritise minimising thermal gradients to ensure the tensile strength of the salt is not exceeded. Additionally, the modelling approach, which uses JFEM with cohesive elements, provides a valuable tool for predicting fracture initiation and can be used to establish safe operating envelopes for different salt formations. Overall, a deeper understanding of coupled thermomechanical behaviour in salt caverns will aid in developing optimised strategies for large-scale hydrogen storage that ensure both structural stability and operational safety.

CRediT authorship contribution statement

Hajar Habbani: Writing – original draft, Visualization, Software, Investigation, Data curation, Conceptualization. **Hippolyte Djizanne:** Writing – review & editing, Writing – original draft, Validation, Resources, Methodology, Investigation, Formal analysis, Conceptualization. **Benoit Brouard:** Writing – review & editing, Visualization, Supervision, Methodology, Formal analysis. **Amade Pouya:** Writing – review & editing, Supervision, Methodology.

Declaration of competing interest

The authors declare that they have no known competing financial interests or personal relationships that could have appeared to influence the work reported in this paper.

Acknowledgments

This research was partly supported by funding from the EU Clean Hydrogen Partnership through the HyPSTER (Grant No. 101006751) and FrHyGe (Grant No. 101137892) projects.

References

Barenblatt, G.I., 1962. The mathematical theory of equilibrium cracks in brittle fracture. Adv. Appl. Mech. 7, 55–129.
Bérest, P., 2011. Thermomechanical Aspects of high-frequency Cycling in Salt Storage Caverns. IGU Research Conference 2011, Seoul, Korea.
Bérest, P., Brouard, B., 1998. A Tentative Classification of Salts According to their

Creep Properties. Proc. SMRI Spring Tech. Conf., New Orleans, USA, pp. 18–38.
Bérest, P., Djizanne, H., Brouard, B., Hévin, G., 2012. Rapid depressurisations: can they lead to irreversible damage? Proc. SMRI Spring Meet., Regina 63–86. Canada.
Bérest, P., Ghoreychi, M., Fauveau, M., Lebitoux, P., 1986. Mechanisms of creep in gas storage caverns: effect of gravity forces. Proceedings of the 27th U.S. Symposium on Rock Mechanics (USRMS), pp. 789–794. Tuscaloosa, USA.
Bérest, P., Sicsic, P., Brouard, B., 2016. Thermomechanical effects of a depressurisation in a CAES cavern. Proc. ARMA/USRMS Symp., 2016 (Paper 16-632), Houston, USA.
Boucly, P., Legreneur, J., 1980. Hydrocarbon storage in cavities leached out of salt formations. In: Proceedings of the International Symposium on Subsurface Space, pp. 251–257. Stockholm.
Brouard, B., Frangi, A., Bérest, P., 2011. Mechanical stability of a cavern submitted to high-frequency cycles. In: Proceedings of the SMRI Spring Meeting. Galveston, USA, pp. 99–116.
Brouard, B., Zakharov, V., Frangi, A., 2022. Numerical modelling of the complex behaviour of salt caverns. In: International Geomechanics Symposium 2022, Abu Dhabi (Paper IGS-2022-028).
Carol, I., Prat, P.C., Lopez, C.M., 1997. Normal/shear cracking model: application to discrete crack analysis. J. Eng. Mech. 123 (8), 765–773.
Chen, Y., Zhou, X., 2022. Scaling behaviour of thermally driven fractures in deep low-permeability formations: a plane strain model with 1-D heat conduction. J. Geophys. Res. Solid Earth 127 e2021JB022964.
Chen, Y., Zhou, X., 2024. Modelling of thermally driven longitudinal fractures along a vertical well. Int. J. Rock Mech. Min. Sci. 175, 105942.
Chen, Y., Zhou, X., 2025. Propagation and arrest of multiple radial thermal fractures transverse to a horizontal well. Int. J. Rock Mech. Min. Sci. 183, 106092.
Coarita-Tintaya, E.-D., Golfier, F., Grgic, D., Souley, M., Cheng, L., 2023. Hydromechanical modelling of salt caverns subjected to cyclic hydrogen injection and withdrawal. Comput. Geotech. 162, 105690.
Coates, G.K., Lee, C.A., McLain, W.C., Senseny, P.E., 1983. Closure and collapse of man-made cavities in salt. In: Proceedings of the 6th International Symposium on Salt, pp. 139–157.
Crotogino, F., Mohmeyer, K.U., Scharf, R., 2001. Huntorf CAES: More than 20 Years of Successful Operation. Proc. SMRI Spring Meet., Orlando, USA, pp. 351–362.
Djizanne, H., 2014. Stabilité mécanique d'une cavité saline soumise à des variations rapides de pression (Thèse de doctorat). École Polytechnique, France.
Djizanne, H., Brouard, B., Hévin, G., 2014. The mechanical stability of a salt cavern used for compressed air energy storage (CAES). In: Proceedings of the SMRI Spring Meeting. San Antonio, USA.
Dreyer, W.E., 1977. Cold and cryogenic storage of petroleum products. In: Proceedings of Rockstore '77 (1St International Symposium on Storage in Excavated Rock Caverns), pp. 237–249. Stockholm.
Dugdale, D.S., 1960. Yielding of steel sheets containing slits. J. Mech. Phys. Solid. 8, 100–104.
Fallah Soltanabad, M.Y., Pouya, A., Brochard, L., Guayacan-Carrillo, L.M., De Lesquen, C., Vu, N.M., 2023. Fluid injection influence on fracture propagation near an underground drift. In: Proceedings of the 15th ISRM Congress and the 72nd Geomechanics Colloquium, Salzburg.
Fracsima, 2016. DISROC User Manual: Finite-Element Code for thermo-hydro-mechanical Modelling in Fractured Media. Fracsima, Paris.
Grgic, D., Al Sahyouni, F., Golfier, F., et al., 2022. Evolution of Gas Permeability of Rock Salt Under Different Loading Conditions and Implications on the Underground Hydrogen Storage in Salt Caverns. Rock. Mech. Rock. Eng 55, 691–714. https://doi.org/10.1007/s00603-021-02681-y.
Hévin, G., Charnavel, Y., Balland, C., et al., 2016. Thermo-mechanical test in a salt mine as part of SMRI research on high-frequency cycling. SMRI Research Report RR2016-1.
Jamshidi, E., Kianoush, P., Hosseini, N., Adib, A., 2024. Scaling-up dynamic elastic logs to pseudo-static elastic moduli of rocks using a wellbore stability analysis approach in the Marun oilfield, SW Iran. Sci. Rep. 14, 19094.
Jin, Z.-H., Sun, C.T., 2006. A comparison of cohesive zone modelling and classical fracture mechanics based on the near-tip stress field. Int. J. Solid Struct. 43, 1047–1060.
Langer, M., 1981. The mechanical behaviour of salt: an overview. In: Proceedings of the 1st Conf. on the Mechanical Behaviour of Salt. Penn State Univ., pp. 131–198
Langer, M., Hunsche, U., Schulze, O., 1984. Analysis of transient creep mechanisms in rock salt. In: Proceedings of the 2nd Conference on the Mechanical Behaviour of Salt. Trans Tech, Clausthal, pp. 185–202.
Lemmon, E.W., Huber, M.L., Leachman, J.W., 2008. Revised standardised equation for hydrogen gas densities for fuel consumption applications. J. Res. NIST 113 (6), 341–350.
Munson, D.E., Dawson, P.R., 1982. A work-hardening/recovery model of transient creep of salt during stress loading and unloading. In: Proceedings of the 23rd U.S. Symposium on Rock Mechanics (USRMS). Berkeley, CA.
Norton, F.H., 1929. Creep of Steel at High Temperature. McGraw-Hill, New York.
Ouraga, Z., Guy, N., Pouya, A., 2017. Modelling of natural fracture initiation and propagation in the basin sedimentation context. J. Geophys. Res. Solid Earth 122, 247–261.
Pellizzaro, C., Bergeret, G., Leadbetter, A., Charnavel, Y., 2011. Thermo-mechanical behaviour of Stublach gas storage caverns. In: Proceedings of the SMRI Fall Meeting. York, UK.
Pirhadi, A., Kianoush, P., Ebrahimabadi, A., Shirinabadi, R., 2023. Wellbore stability in a depleted reservoir by finite element analysis of coupled thermo-poro-elastic units in an oilfield, SW Iran. Results Earth Sci 1, 100005.
Pirhadi, A., Kianoush, P., Varkouhi, S., Shirinabadi, R., Shirazy, A., Shirazi, A., Ebrahimabadi, A., 2025. Thermo-poroelastic analysis of drilling fluid pressure and temperature on wellbore stresses in the Mansouri oilfield, SW Iran. Results Earth Sci 3, 100061. https://doi.org/10.1016/j.rines.2025.100061.
Pouya, A., 1991a. Correlation between mechanical behaviour and petrological properties of rock salt. In: Proceedings of the 32nd U.S. Symposium on Rock Mechanics. Balkema, pp. 385–392.
Pouya, A., 1991b. Comportement rhéologique du sel gemme – application à l'étude des excavations souterraines (Thèse de doctorat). ENPC, France.
Pouya, A., Bemani, P.Y., 2015. A damage-plasticity model for cohesive fractures. Int. J. Rock Mech. Min. Sci. 73, 194–202.
Quast, P., 1983. L'installation de Huntorf : plus de trois années de fonctionnement de cavernes à air comprimé. Ann. Mines 190 (5–6), 93–102.
Röhr, H.U., 1974. Mechanical behaviour of a gas storage cavern in evaporite rocks. Proceedings of the 4th Symposium on Salt 2, 93–100.
Silberschmidt, V.G., Silberschmidt, V.V., 2000. Analysis of cracking in rock salt. Rock Mech. Rock Eng. 33 (1), 53–70.
Tijani, M., 1989. COSA II: further benchmark exercises to compare geomechanical computer codes for salt. Atkins Engineering Report.
Tounsi, H., Pouya, A., Rohmer, J., 2020. Coupled hydro-chemo-mechanical model for fault activation under reactive fluid injection. Eur. J. Environ. Civil Eng. https://doi.org/10.1080/19648189.2020.1832583.
Trivellato, E., Pouya, A., Vu, M.-N., Seyedi, D., 2018. Damage-based cohesive modelling for fracture initiation and propagation around a deep tunnel in quasi-brittle rocks. In: Zhang, L., Gonçalves da Silva, B., Zhao, C. (Eds.), Proceedings of GeoShanghai 2018 International Conference: Rock Mechanics and Rock Engineering. Springer, Singapore.
Wallner, M., Eickemeier, R., 2001. Subsidence and fractures caused by thermo-mechanical effects. In: Proceedings of the SMRI Spring Meeting, pp. 363–371. Orlando, USA.
Wang, T., Hou, L., Li, X., Lü, Q., 2016. Experimental study on mode-I fracture toughness and energy release rate of bedded rock salt. Chin. J. Rock Mech. Eng. 35 (8), 1553–1560 (in Chinese).
Wang, T., Yang, C., Chen, J., Daemen, J.J.K., 2018. Geomechanical investigation of roof failure in China's first gas storage salt cavern. Eng. Geol. 243, 59–69.
Wawersik, W.R., Zeuch, D.H., 1984. Creep and Creep Modelling of Three Domal Salts: a Comprehensive Update. Sandia National Laboratories Report SAND84-0568.
Zapf, D., Staudtmeister, K., Rokahr, R.B., 2012. Analysis of thermally induced fractures in salt. In: Proceedings of the SMRI Spring Meeting, pp. 47–61. Regina, Canada.



Hajar Habbani is a PhD candidate at the French National Institute for Industrial Environment and Risks, Verneuil-en-Hallate, France, since January 2024. She holds a Master of Science from CentraleSupélec, Paris-Saclay University, France, in Civil Engineering, with a specialisation in geotechnics, geomechanics, and underground structures. She also earned a degree in Civil Engineering from the National School of Applied Sciences in Morocco. Her doctoral research focuses on the analysis of damage and fracture processes induced in salt caverns, with a particular application to underground hydrogen storage (UHS). She investigates the thermo-hydromechanical behaviour of salt caverns under cyclic pressure and temperature loading, with emphasis on fracture initiation, propagation, and cavern integrity. Her research combines numerical modelling of the fracture process for UHS risk assessment with experimental work to identify fracture parameters in rock salt.